

1

2

3

4

# Storage and Transport of Charge in Redox Conductive Polymers Probed with Electron Spin Resonance Spectroscopy

5

**Ilia Romanovich Kulikov**

6

7

8

Im Fachbereich Physik der Freien Universität Berlin eingereichte  
Dissertation zur Erlangung des Grades eines  
Doktors der Naturwissenschaften

9

10

Berlin  
August 2023

11

12

13

14

Erster Gutachter: Prof. Dr. Jan Behrends

Zweiter Gutachter: Prof. Dr. Kirill Bolotin

Tag der Disputation:

# Contents

16	<b>1 Introduction</b>	7
17	<b>2 Electrochemical Energy Storage in Redox Conductive Polymers</b>	9
18	2.1 Redox Conductive Polymers . . . . .	9
19	2.2 Organic Radical Battery . . . . .	9
20	2.3 TEMPO-Salen Cathode Material . . . . .	10
21	<b>3 Operando EPR Spectroscopy of TEMPO-Salen Cathode Films</b>	11
22	3.1 Electron Paramagnetic Resonance . . . . .	11
23	3.1.1 The Spin Hamiltonian . . . . .	11
24	3.1.2 Instrumentation . . . . .	12
25	3.2 EPR Spectroscopy of a Charging Electrochemical Cell . . . . .	12
26	3.2.1 Fabrication of EPR-compatible Electrochemical Cells . . . . .	13
27	3.2.2 cwEPR Spectra During a Charge-Discharge Cycle . . . . .	13
28	3.2.3 Spectral Simulations . . . . .	14
29	3.2.4 Quantitative Analysis of Potential-Dependent EPR Spectra . . . . .	14
30	3.2.5 EPR-Detected State Of Charge . . . . .	14
31	3.2.6 Formation of Singlet Spin States in a Reduced Cathode Film . . . . .	14
32	3.2.7 Monitoring of Degradation Processes . . . . .	14
33	3.2.8 Monitoring of Self Discharge . . . . .	14
34	3.2.9 Electrochemical Cells with Solid Electrolyte . . . . .	14
35	3.2.10 Low Temperature Measurements . . . . .	14
36	<b>4 pEPR Spectroscopy of Densely Packed Nitroxide Radicals</b>	17
37	4.1 Coherent Spin Motion under Pulsed Microwave Field . . . . .	17
38	4.1.1 Bloch Equations . . . . .	17
39	4.1.2 Spin Relaxation Times . . . . .	17
40	4.1.3 Spin Packets . . . . .	17
41	4.2 Instrumentation . . . . .	17
42	4.2.1 Pulse Sequences and Measurement Techniques . . . . .	17
43	4.2.2 Broad-Band Excitation and Instantaneous Diffusion . . . . .	18
44	4.3 Pulsed EPR Spectroscopy of a charged pDiTBuS Cathode film . . . . .	18
45	4.3.1 Field Swept Echo of a charged pDiTBuS Cathode film . . . . .	18
46	4.3.2 Estimation of Local Spin Concentrations with Instantaneous Diffusion . . . . .	18
47	4.3.3 Spin Relaxation in a charged pDiTBuS Cathode Film . . . . .	18
48	4.3.4 Pade-Laplace Deconvolution of Echo Decay Transients . . . . .	18
49	4.3.5 Detection of Domains with Poor Conductivity . . . . .	18
50	4.3.6 Towards Imaging of Spin Concentration in Battery Electrodes . . . . .	18
51	4.3.7 Unusual Peak Ratios in a Highly Charged Cathode Film . . . . .	19
52	<b>5 Longitudinally Detected Electron Paramagnetic Resonance in Systems with Short Relaxation Times</b>	21

54	<b>6 Electrically Detected Magnetic Resonance on a Cathode of an Organic Radical Battery</b>	23
55	6.0.1 Spin Blockade and Spin-Dependent Recombination . . . . .	23
56	6.0.2 Instrumentation . . . . .	23
57	6.0.3 Device Fabrication . . . . .	23
58	6.0.4 EDMR signal in a 1N4007 Si Diode . . . . .	24
59	6.0.5 EDMR signal in an Organic Field Effect Transistor . . . . .	24
60	6.0.6 EDMR signal in a TEMPO-Salen Electrochemical Cell . . . . .	24
61	6.0.7 Distribution of Current Density in On-Substrate Meander-Shaped Electrodes . . . . .	24
62	<b>7 The Deep-Trap Model of a TEMPO-Salen Electrode Film</b>	27
63	<b>8 Conclusions and Outlook</b>	29

---

$\vec{e}_x, \vec{e}_y, \vec{e}_z, t$	Laboratory frame of reference
$\hat{\vec{S}} = (\hat{S}_x, \hat{S}_y, \hat{S}_z)$	Spin operator
$h = 6.62607015 \times 10^{-34} \text{ J} \times \text{s}$	Planck constant
$g_e = -2.00231930436118(27)$	Electron g factor
$\mu_B = 9.2740100783(28) \times 10^{-24} \text{ J/T}$	Bohr magneton
$\mu_0 = 1.25663706212(19) \times 10^{-6} \text{ N/A}^2$	Permeability of free space
$\epsilon$	Relative permittivity
$\vec{B}_0 = B_0 \vec{e}_z$	Static magnetic field
cwEPR	Continuous wave electron paramagnetic resonance
pEPR	Pulsed electron paramagnetic resonance
EDMR	Electrically detected magnetic resonance
DUT	Device under testing
ORB	Organic radical battery
WE	Working electrode (cathode, “+”)
CE	Counter electrode (anode, “-”)
RE	Reference electrode
SoC	State of charge
ESOC	EPR-detected SoC
CV	Cyclic voltammogram
GCD	Galvanostatic charge-discharge
TEMPO	2,2,6,6-tetramethylpiperidine-1-oxyl
pDiTS	Poly-di-TEMPO-Salen
pDiTBuS	Poly-di-TEMPO-Butyl-Salen
PTMA	Poly-TEMPO-methacrylate
EDFS	Echo-detected field sweep
ID	Instantaneous diffusion
$T_1$	Spin-lattice relaxation time
$T_m$	Phase memory time
$t_d$	Microwave detector dead time

---

Table 1: List of abbreviations



<sup>64</sup> **Chapter 1**

<sup>65</sup> **Introduction**

<sup>66</sup> Life needs energy to continue its spread. Plants use photosynthesis to separate carbon from oxygen  
<sup>67</sup> and to grow. Higher life forms as humans consume energy during the day and during the night, being  
<sup>68</sup> dependent on the available energy source [?]. While fossil fuels are still the major source of energy [?]  
<sup>69</sup> and while fire is used to convert the Joules that hold together hydrocarbon molecules into a "horse power"  
<sup>70</sup> of a combustion engine and kilowatt-hours in a power socket, there are cleaner and more efficient ways  
<sup>71</sup> to harvest energy. Photosynthesis had inspired the creation of solar panels that convert the sunlight into  
<sup>72</sup> electricity, the atom had been tamed in the core of a nuclear reactor to power cities; we can extract energy  
<sup>73</sup> from sound [?], wind and waves and from the heat of the planet. Moreover, there are hopes and contin-  
<sup>74</sup> uous attempts to achieve nuclear fusion [?] - the creation of an artificial Sun by melting together atomic  
<sup>75</sup> cores - the virtually inexhaustible and clean source of energy. The oil and gas are limited and unevenly  
<sup>76</sup> distributed resources, wind does not always blow, the Sun does not shine at night, the wild Nature is still  
<sup>77</sup> unpredictable and the extracted energy has to be stored in order to level out its production and consumption.

<sup>78</sup>

<sup>79</sup> With the rise of the technological era, over the last century, energy has been delivered to our homes in  
<sup>80</sup> form of electricity. Energy storage systems such as fuel cells, supercapacitors and batteries are crucial ele-  
<sup>81</sup> ments for powering portable electronics and vehicles, or for balancing a power grid with a renewable energy  
<sup>82</sup> source. [15]. Two opposite electric charges separated from each other can store energy in an electrostatic  
<sup>83</sup> field. It is possible to accumulate many charges on the plates of a capacitor and store some energy [?], but  
<sup>84</sup> due to the technological difficulties, electrochemical cells are commonly used instead. An electrochemical  
<sup>85</sup> cell is an energy storage device and a power source that undergoes a chemical reaction to transfer some  
<sup>86</sup> electric charge from one of its components to another through an external circuit. A simple electrochemical  
<sup>87</sup> cell consists of three elements: two spatially separated materials called electrodes, and a solution of mobile  
<sup>88</sup> ions between them called electrolyte. The two electrodes have different work functions, or, chemically  
<sup>89</sup> speaking, reduction-oxidation (redox) potentials. When the electrodes of the cell are connected through  
<sup>90</sup> an external circuit, the electrons flow through the circuit and the ions in the electrolyte rearrange to main-  
<sup>91</sup> tain charge balance [31]. While the cell delivers the electric current to the circuit, a chemical reaction is  
<sup>92</sup> happening on its electrodes: the positively charged electrode, called cathode, is being reduced, obtaining  
<sup>93</sup> electrons from the negatively charged anode through the external circuit. The anode loses electrons and  
<sup>94</sup> is being oxidized. If the electrodes can undergo a reversible redox reaction, a current applied to the cell  
<sup>95</sup> restores its charged state. The speed, reversibility, released by-products and physical conditions of this  
<sup>96</sup> redox reaction are the key factors that define the charging rate, cycling stability, the self-discharge rate and  
<sup>97</sup> the area of application of an electrochemical cell. This type of redox reaction had been of great interest  
<sup>98</sup> for the field of energy storage, particularly, electrochemistry [?], where numerous characterization tech-  
<sup>99</sup> niques have been developed to optimize the architecture of electrochemical power sources. Depending on  
<sup>100</sup> the redox potentials of the used electrodes, the output voltage of a cell ranges between 0 and 5 V. Most  
<sup>101</sup> applications require higher voltages, so multiple cells are connected in series to form a battery.

<sup>102</sup>

103 Stable, capacious and powerful batteries have become of great demand for today's energy driven so-  
104 ciety [51, 50, 36]. The advances in lithium ion technology for rechargeable batteries have enabled en-  
105 ergy densities that make it possible to battery-power a wearable Internet-of-things device [24, 28], an  
106 airplane [19] or a house [4, 13]. Still, the application of lithium ion batteries is limited by irreversible  
107 processes [23, 8, 55] that occur upon extreme operating conditions such as high power demand [54, 12]  
108 or over-discharge [27]. Such degradation processes limit the performance of a battery by lowering its safe  
109 operating power, resulting in lower power density and longer charging times. The challenge to overcome  
110 these limitations, together with low abundance of Lithium, Cobalt and rare earth metals, [50, 15] and the  
111 toxicity of the manufacturing process [38, 37] is motivating research and development of advanced battery  
112 technologies [3]. This requires understanding of charge transport and degradation pathways in energy stor-  
113 age materials as well as exploring novel materials such as materials based on organic precursors [26, 20].

114 The flexible molecular design together with questions regarding unresolved charge transport- and per-  
115 formance limiting mechanisms have inspired a variety of characterization techniques to be developed and  
116 applied to both energy storage materials and energy storage devices, operando and ex-situ. Together  
117 with electrochemical characterization as the standard method for studying the properties of energy stor-  
118 age materials[45, 53], operando optical microscopy [30], neutron imaging [27] and X-ray diffraction [39]  
119 were applied to monitor irreversible structural deformations during extreme charging of Li cells.

120 UV and IR spectroscopy turned out to be particularly useful for studying organic energy-storage ma-  
121 terials. For instance, it was possible to observe formation of positive polarons in the NiSalen backbone  
122 of the pDiTBuS upon its oxidation [5]. Since the electrochemical processes happen within the bulk of  
123 the energy storage material and involve changes in the spin states, imaging techniques based on mag-  
124 netic resonance can be applied to obtain structural information on the battery electrodes on the molecular  
125 level [34, 29, 25, 1]. NMR was used to study dendrite formation, electrolyte dynamics and intercalation of  
126 Li ions[22, 11] in Li cells, including operando imaging [44].

127 Operando continuous-wave EPR (cwEPR) was applied to study redox kinetics of inorganic battery  
128 cathodes [33], radical formation and spin densities in redox polymers [5] and in organic electrochemical  
129 cells [14, 21].

130 Pulsed EPR (pEPR) provides an even more powerful toolbox for material studies with the electron spin  
131 as a microscopic structural probe. In particular, pEPR provides access to the dipolar coupling between  
132 neighboring electron spins and thus the possibility to determine distances between adjacent redox-active  
133 centers using dipolar spectroscopy [40] as in spin-labelled proteins [18, 46]. In addition, the hyperfine  
134 coupling between electron and nuclear spins in close vicinity can be measured by electron spin echo en-  
135 velope modulation (ESEEM) and electron nuclear double resonance (ENDOR) techniques and can thus  
136 elucidate the degree of delocalization for charge carriers in ORB materials in a similar way as in organic  
137 semiconductors [6].

138 **EDMR** is allowing to manipulate the spin of an electron that tunnels through a disordered media such as  
139 the amorphous silicon in a solar cell, through intertwined fragments of conjugated polymers in an organic  
140 solar cell or an organic field-effect transistor.

<sup>142</sup> **Chapter 2**

<sup>143</sup> **Electrochemical Energy Storage in  
Redox Conductive Polymers**

<sup>145</sup> **2.1 Redox Conductive Polymers**

<sup>146</sup> A  $\pi$  - conjugated network, such as polyacetylene, exhibits a band structure in the electron energy levels and  
<sup>147</sup> represents a molecular semiconductor.

<sup>148</sup> After the discovery of the conductivity of polyacetylene by XXXXX in 1970s, [] the field of organic  
<sup>149</sup> electronics has expanded dramatically. Organic solar cells and organic field effect transistors contain con-  
<sup>150</sup> jugated polymers that have electrical properties of semiconductors, yet can be easily printed in form of thin  
<sup>151</sup> flexible films without using high temperatures.

<sup>152</sup> **2.2 Organic Radical Battery**

<sup>153</sup> Batteries based on conjugated polymers containing stable radical moieties as high-capacitance groups rep-  
<sup>154</sup> resent a promising class of future electrochemical power sources - organic radical batteries (ORB) [32, ?, ?,  
<sup>155</sup> ?]. ORB combine the advantages of high-power supercapacitors, namely high discharge rates, and the high  
<sup>156</sup> energy density of conventional lithium-ion technology. In contrast to the lithium-ion battery, the charging  
<sup>157</sup> of an organic battery does not involve intercalation of metal ions into the electrodes. This reduces the struc-  
<sup>158</sup> tural change of the electrode upon repeated recharging which allows for a longer cycle life of an ORB. The  
<sup>159</sup> semi-conducting nature of organic electrodes reduces the Joule heating during the battery operation, and  
<sup>160</sup> this allows for higher charge/discharge rates. The amorphous and swollen structure of organic electrodes  
<sup>161</sup> allows the electrolyte ions to diffuse faster into the electrode, which also increases the charge/discharge  
<sup>162</sup> rate [35]. A further beneficial property of organic materials over traditional inorganic materials is their  
<sup>163</sup> availability and the low cost of the starting materials for the synthesis of the target polymers in conjunction  
<sup>164</sup> with good mechanical properties [15, 31, 7]. The large knowledge base on polymer processing allows for  
<sup>165</sup> inkjet printing, roll-to-roll processing and other low-cost manufacturing techniques for making low-cost,  
<sup>166</sup> flexible and light-weight integrated devices, including flexible plastic batteries [15, 35].

<sup>167</sup> **Organic Electrode Materials**

<sup>168</sup> ORB based on redox polymers containing stable radicals [32] have been shown to compete with or even  
<sup>169</sup> outperform conventional Li based batteries in terms of power densities [45] with the additional benefit of  
<sup>170</sup> being free from rare precursors, inheriting mechanical properties of plastics and electrical properties of  
<sup>171</sup> semiconductors [7, 2, 10]. Advanced molecular design techniques allow for tuning of the electrochemical  
<sup>172</sup> properties of the redox polymers [16], that brings in a rich variety of organic energy storage materials [49,  
<sup>173</sup> 48, 17] and creates a large room for their optimization.

<sup>174</sup> While active electrode materials with nitroxide radicals as redox-active groups are ideally suited for  
<sup>175</sup> organic radical batteries (ORBs) that exhibit high power densities, the broad application of most nitroxide-

based materials is limited by their moderate electrical properties. A promising route towards overcoming the conductivity problem is the use of polymers that combine radical-containing moieties and a conductive backbone. This strategy was successfully followed in a number of studies focusing on different polymers.[?, ?, ?, ?, ?, ?]

### 2.3 TEMPO-Salen Cathode Material

Redox conductive conjugated polymers containing TEMPO (2,2,6,6-tetramethylpiperidine-1-oxyl) redox groups, as pDiTBuS (poly-di-TEMPO-Butyl-Salen) shown in Figure 2.1, demonstrate particularly promising energy and power densities [47]. The pDiTBuS was designed as a cathode material: it is oxidized when the electrochemical cell containing this material is charged. A film of pDiTBuS comprises a high concentration of redox active stable nitroxyl radicals attached to a conjugated polymer backbone that interconnects them as a molecular wire. Such system may be viewed as a highly disordered molecular hole-transporting semiconductor (the poly-NiSalen backbone) that contains a large amount of hole traps (TEMPO groups) attached to it with butyl linkers. When the film is reduced (discharged), the TEMPO groups are in the radical state and act as unfilled traps. Upon oxidation (charging), the TEMPO fragments lose an unpaired electron and acquire a positive charge, so the traps are being filled with holes.

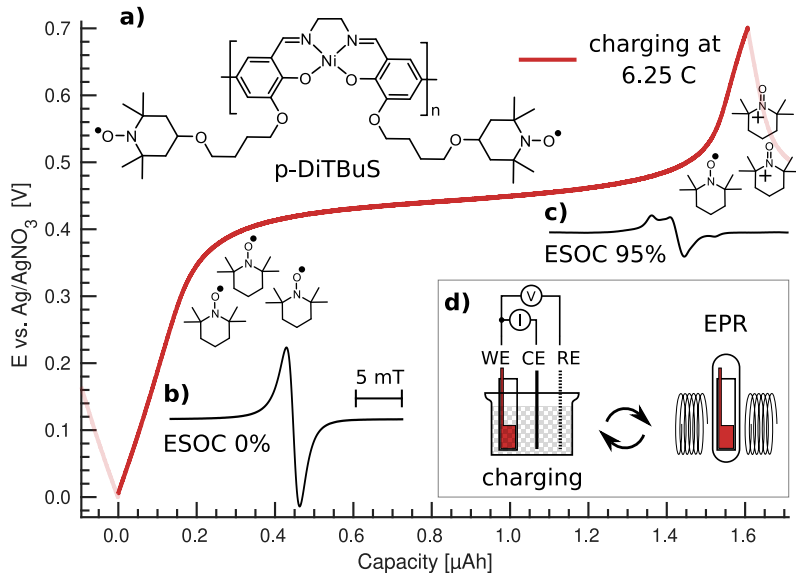


Figure 2.1: Galvanostatic charge-discharge curve for a pDiTBuS cathode film at 10  $\mu$ A (6.25 C), chemical structure of pDiTBuS (a), normalized cwEPR spectral signatures for reduced (b) and oxidized (c) states. Scheme of the ex-situ EPR measurement on the pDiTBuS half cell (d).

<sup>191</sup> **Chapter 3**

<sup>192</sup> **Operando EPR Spectroscopy of  
TEMPO-Salen Cathode Films**

<sup>194</sup> **3.1 Electron Paramagnetic Resonance**

<sup>195</sup> **3.1.1 The Spin Hamiltonian**

<sup>196</sup> **Electron Spin** The electron bears an internal angular momentum that is called spin. Spin combines with  
<sup>197</sup> the charge of the electron to endow the electron with a magnetic moment. The magnetic moment of the  
<sup>198</sup> electron is quantized:  $\mu_e = \mu_B g S$  [9], where  $S$  is the spin quantum number, the eigenvalue of the spin  
<sup>199</sup> operator  $\hat{S}$ , that equals  $S = 1/2$  for an electron. When an electron is placed in a static magnetic field  
<sup>200</sup>  $\vec{B}_0 = B_0 \hat{e}_z$ , its magnetic moment precesses about the field direction with the Larmor frequency  $\omega_L = \gamma B_0$ ,  
<sup>201</sup> where  $\gamma = \frac{g_e \mu_B}{\hbar} = 28.025$  GHz/T is the gyromagnetic ratio of the electron and  $g_e$  is the electron g factor.  
<sup>202</sup> The projection of the electron's magnetic moment on the direction of the magnetic field can take only  
<sup>203</sup> discrete values between  $-S = -1/2$  and  $S = 1/2$ , so that the eigenvalues of the  $z$  component of the spin  
<sup>204</sup> operator are also discrete:  $\hat{S}_z |\uparrow\rangle = +\frac{\hbar}{2} |\uparrow\rangle$ ,  $\hat{S}_z |\downarrow\rangle = -\frac{\hbar}{2} |\downarrow\rangle$ . The two eigenfunctions of  $\hat{S}_z$  are called the  
<sup>205</sup> spin-up state  $|\uparrow\rangle$  and the spin-down state  $|\downarrow\rangle$ . The two corresponding eigenvalues  $\pm \frac{\hbar}{2}$  define the energy  
<sup>206</sup> difference between the states  $|\uparrow\rangle$  and  $|\downarrow\rangle$ , that is known as the Zeeman splitting.

<sup>207</sup> **Zeeman Splitting** The energy of an unpaired electron placed in the external magnetic field  $\vec{B}_0$  is the  
<sup>208</sup> eigenvalue of the spin Zeeman Hamiltonian:  $\hat{H}_{EZ} = \mu_B g \vec{B}_0 \cdot \vec{S}$ . In the laboratory frame of reference  $\vec{B}_0 \parallel \hat{e}_z$ ,  
<sup>209</sup>  $[\hat{H}_{EZ}, \hat{S}_z] = 0$ , so  $\hat{H}_{EZ}$  and  $\hat{S}_z$  share the two eigenfunctions  $|\uparrow\rangle$  and  $|\downarrow\rangle$ . The Zeeman energies of the electron  
<sup>210</sup> are  $E_{EZ}^{\pm} = \pm \frac{\hbar}{2} \mu_B g B_0$ .

<sup>211</sup> **Nuclear Spin and Nuclear Zeeman Splitting** A proton also bears an internal angular momentum  $S =$   
<sup>212</sup>  $1/2$  that results in a magnetic moment  $\mu_p = \mu_e \frac{m_e}{m_p}$ , that is  $\frac{m_e}{m_p} \approx 1836$  times smaller than the electron's  
<sup>213</sup> magnetic moment. A neutron bears no charge but still has an internal angular momentum  $S = 1/2$ . An  
<sup>214</sup> atomic nucleus that consists of protons and neutrons can have a magnetic moment, depending on the  
<sup>215</sup> mutual orientations of their spins and on the nuclear charge. A nitrogen nucleus has 7 protons and 7  
<sup>216</sup> neutrons that total in a nuclear spin  $I = 1$  which, with the g factor for the nitrogen nucleus  $g_N$ , results in the  
<sup>217</sup> nuclear magnetic moment of  $\mu_N = \mu_B g_N \frac{m_e}{m_N} I$  that splits into three Zeeman energy levels corresponding to  
<sup>218</sup>  $I = -1, 0, +1$ , analogously to the electron with  $S = 1/2$ . The nuclear Zeeman splitting is more than three  
<sup>219</sup> orders of magnitude weaker than the electron Zeeman splitting because of the difference in the masses of  
<sup>220</sup> the particles.

<sup>221</sup> **Hyperfine Interaction** The magnetic moments of an electron and a magnetic nucleus, such as nitrogen,  
<sup>222</sup> couple in the hyperfine interaction [42]:  $H_{HF} = \vec{S} \mathbf{A} \vec{I} = H_F + H_{DD}$  with the hyperfine tensor  $\mathbf{A}$ . The

isotropic part  $H_F = a_{iso}\vec{S}\vec{I}$ , or the Fermi contact interaction, scales with the probability density of the electron at the position of the nucleus  $a_{iso} = \frac{2}{3}\frac{\mu_0}{\hbar}g_e\beta_e g_n\beta_n|\psi(0)|^2$ . The anisotropic part  $H_{DD} = \vec{S}\vec{T}\vec{I}$  with the dipolar coupling tensor  $\mathbf{T}$  takes into account the anisotropic dipole-dipole coupling between the magnetic moments of the electron and the nucleus.

**Nuclear Quadrupole Moment** The nitrogen nucleus has a spin greater than 1/2 which alters the charge distribution within the nucleus which gives rise to a non-vanishing nuclear electrical quadrupole moment  $Q$ . The interaction between the asymmetrically distributed charge and the gradient of the electric field at the nucleus is given by the nuclear quadrupole Hamiltonian  $H_{NQ} = \vec{I}\vec{\mathbf{P}}\vec{I}$  with the nuclear quadrupole tensor  $\mathbf{P}$  that describes the coupling of the nuclear quadrupole moment to the electric field gradient.

**Exchange Interaction** In a system of closely placed electrons, such as in a film of densely packed nitroxide radicals, the electron orbitals may overlap significantly and the radicals may exchange electrons. The energy required to exchange the electrons is called the Heisenberg exchange coupling  $H_{exch} = \vec{S}_1\mathbf{J}\vec{S}_2$ , that becomes considerably large at inter-spin distances below  $r < 1.5$  nm or with a large spin delocalization [43]. The positive  $\mathbf{J}$  corresponds to a weak coupling between  $S_1$  and  $S_2$  which leads to an antiferromagnetic or antiparallel alignment of spins with a total  $S = 0$ , whereas the negative  $\mathbf{J}$  causes the strong inter-spin coupling which leads to a ferromagnetic alignment with  $S = 1$ .

**Magnetic Dipole-Dipole Interaction** The dipole-dipole interaction between the two neighboring electron spins contributes one more term to the spin Hamiltonian:  $H_{dd} = \vec{S}_1\vec{\mathbf{D}}\vec{S}_2$  that depends on the distance between the spins.

### 3.1.2 Instrumentation

**EPR Hardware** First observed in 1944 [52, 41], the phenomenon of electron paramagnetic resonance had become a tool for probing local molecular environments in species that contain an unpaired electron. A free electron, that does not interact with its environment and has  $g = g_e$ , experiences a Zeeman splitting of  $\Delta E = g\mu_BB_0$ , that corresponds to the energy of a photon with a frequency of  $\nu = \Delta E/h$ . At  $B_0 \approx 0.3$  T, a microwave photon with  $\nu \approx 9.5$  GHz can drive the magnetic dipole transition between  $|\uparrow\rangle$  and  $|\downarrow\rangle$ , that is called the spin flip. The microwave sources are historically[?] available in a number of discrete bands, one of them is known as  $X$  band for the range between 8 and 12 GHz. To ensure that only the magnetic component of the microwave photon is interacting with the sample, a resonating cavity is used, where a standing microwave is formed, so that in the center of the cavity, the magnetic component of the microwave is maximized and the electric component is quenched. The sample is inserted in the center of the cavity and the external magnetic field is swept. When the resonance condition is met ??, the spin flip occurs and the photon is being absorbed by the sample. The resonance absorption of microwaves can be detected by a small decrease in the quality factor  $Q$  of the resonating cavity, as the magnetic field is being scanned and the microwave frequency is kept constant. The change in the  $Q$  factor during the spin flip leads to temporal decoupling of the resonator, that causes reflections of the microwave that would have entered the resonator off resonance. The intensity of the microwaves is measured with a biased semiconductor diode that has a linearly changing conductivity in the range corresponding to the incident microwave power. A phase sensitive detection with the shallow modulation of  $B_0$  increases the signal-to-noise ratio (SNR), and yields the derivative of the resonance absorption profile. The typically high  $Q \gg 1$  factor of the resonating cavity further increases the SNR.

## 3.2 EPR Spectroscopy of a Charging Electrochemical Cell

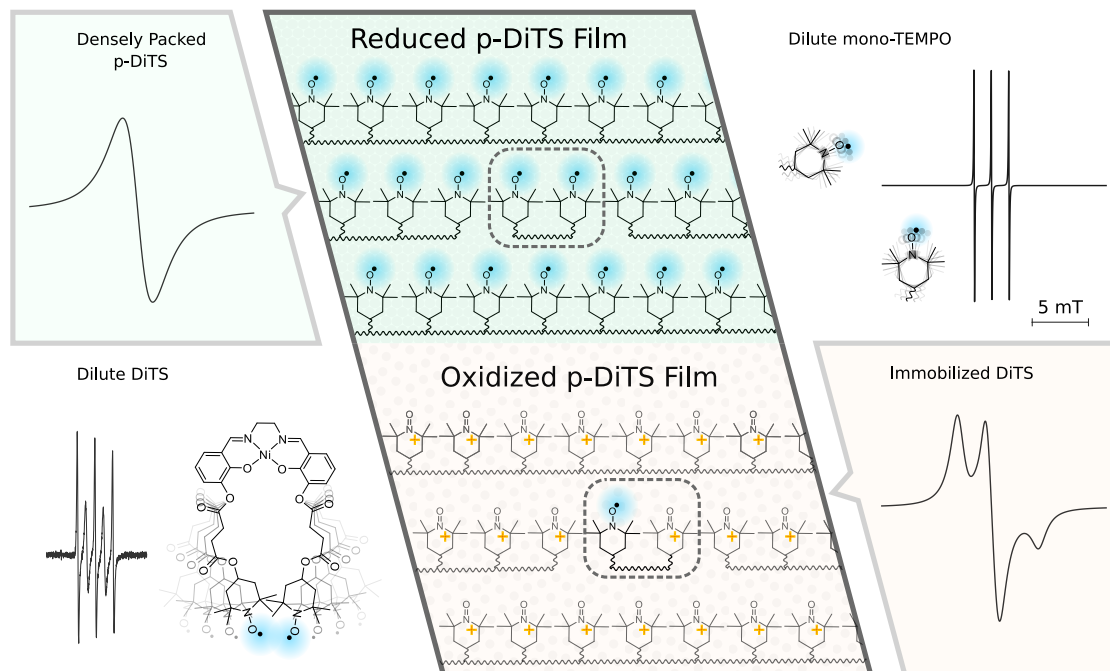
There is a number of difficulties when it comes to an EPR experiment on a working electrochemical cell. The cell must contain mobile ions between its electrodes. The ions are normally produced as products of dissociating salts. To overcome break the salt into the ions (a cation and an anion), a solvent with large

267 dipole moment is needed. Solvents with large dipole moments, as acetonitrile ( $\text{CH}_3\text{CN}$ ,  $\epsilon \approx 37.5$ ) or water  
 268 ( $\epsilon \approx 78.4$ ), have large dielectric constants which results in a non-resonant absorption of microwaves. A  
 269 cell containing liquid electrolyte absorbs microwaves and lowers the sensitivity of the EPR experiment.  
 270 Furthermore, due to a finite dimension of cell, not only the magnetic component of the microwave is  
 271 interacting with the electrolyte, but also the electric one - this results in heating of the electrolyte in a  
 272 similar fashion as in a microwave oven. The heating of the electrolyte leads to a faster degradation of the  
 273 cell and does not allow for long systematic measurements.  
 274 Another general issue with the operando EPR and EDMR experiments is that the device under testing  
 275 (DUT) has to have metal electrodes that deliver current to it. Metals, placed in a microwave cavity, change  
 276 the distribution of the electromagnetic field in it - that weakens the magnetic component at the device and  
 277 at the same time strengthens the electric component. It is the magnetic dipole transition that is causing  
 278 the magnetic resonance, so the weakening of the magnetic component by introducing the metal electrodes  
 279 further decreases the magnetic resonance response. The increased electric component causes heating to  
 280 temperatures that can be critical for the DUT operation.

### 281 3.2.1 Fabrication of EPR-compatible Electrochemical Cells

### 282 3.2.2 cwEPR Spectra During a Charge-Discharge Cycle

283 There are four characteristic cwEPR signatures of an electrochemical cell containing di-TEMPO-Salen  
 284 polymer cathode. The well known signature of a freely tumbling TEMPO<sup>•</sup> exhibits three narrow lines  
 corresponding to the three nuclear sublevels of nitrogen:  $m_I = -1, 0, +1$ .



285 Figure 3.1: XXX

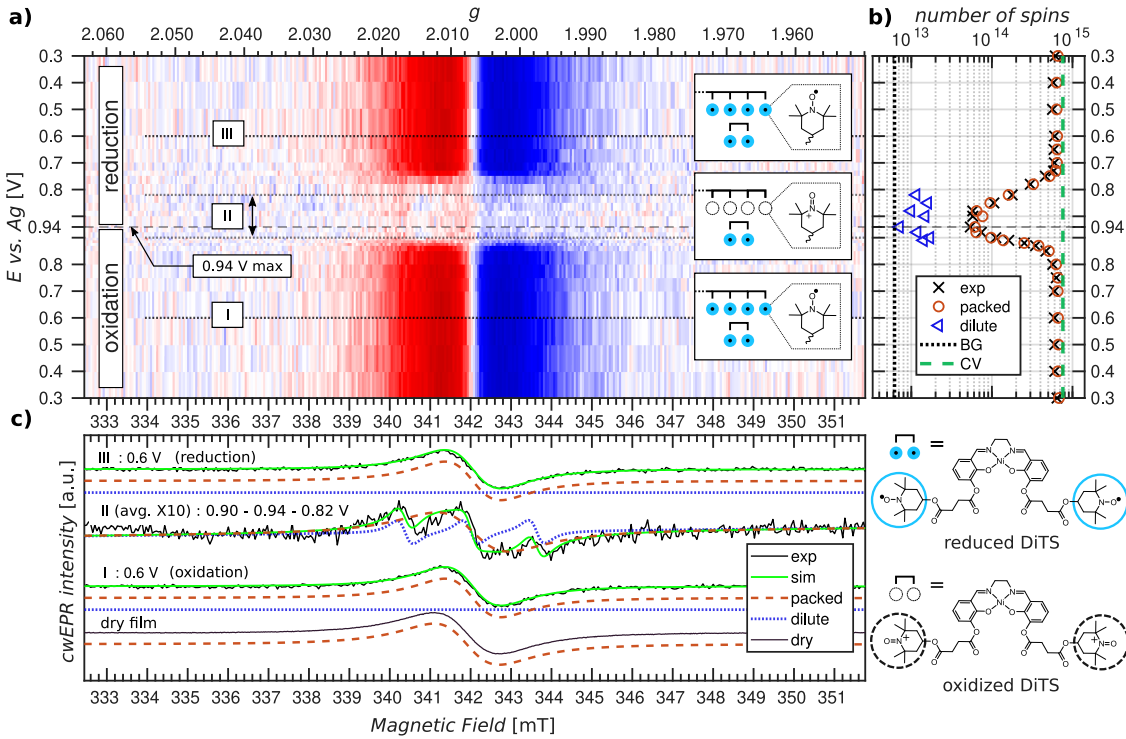


Figure 3.2: XXX

286 **3.2.3 Spectral Simulations**

287 **3.2.4 Quantitative Analysis of Potential-Dependent EPR Spectra**

288 **3.2.5 EPR-Detected State Of Charge**

289 **3.2.6 Formation of Singlet Spin States in a Reduced Cathode Film**

290 **3.2.7 Monitoring of Degradation Processes**

291 **3.2.8 Monitoring of Self Discharge**

292 Organic Radical Batteries have a tendency to self-discharge, as the organic electrochemically active layer  
 293 partially dissolves in polar electrolytes. Particularly for the TEMPO containing ORB, the dissolved, mobile  
 294 TEMPO fragments serve as redox shuttles that carry the charge between the battery electrodes and  
 295 cause a self discharge. The amount of unoxidized TEMPO<sup>•</sup> shuttles can be measured with cwEPR spec-  
 296 troscopy as the mobile fragments have distinct spectra as compared to the fragments tightly packed in the  
 297 electrode. Further in this subsection operando spectra of a TEMPO containing electrochemical cells are  
 298 shown. Quantitative analysis of the released fragments during a charge-discharge cycle allows for a de-  
 299 scription of the self-discharge process in an ORB. The charge state of a battery is monitored with cwEPR  
 300 and, additionally, with a potentiometric measurement to identify the self-discharge rate and to connect it  
 301 with the concentration of diffusing redox shuttles.

302 **3.2.9 Electrochemical Cells with Solid Electrolyte**

303 **3.2.10 Low Temperature Measurements**

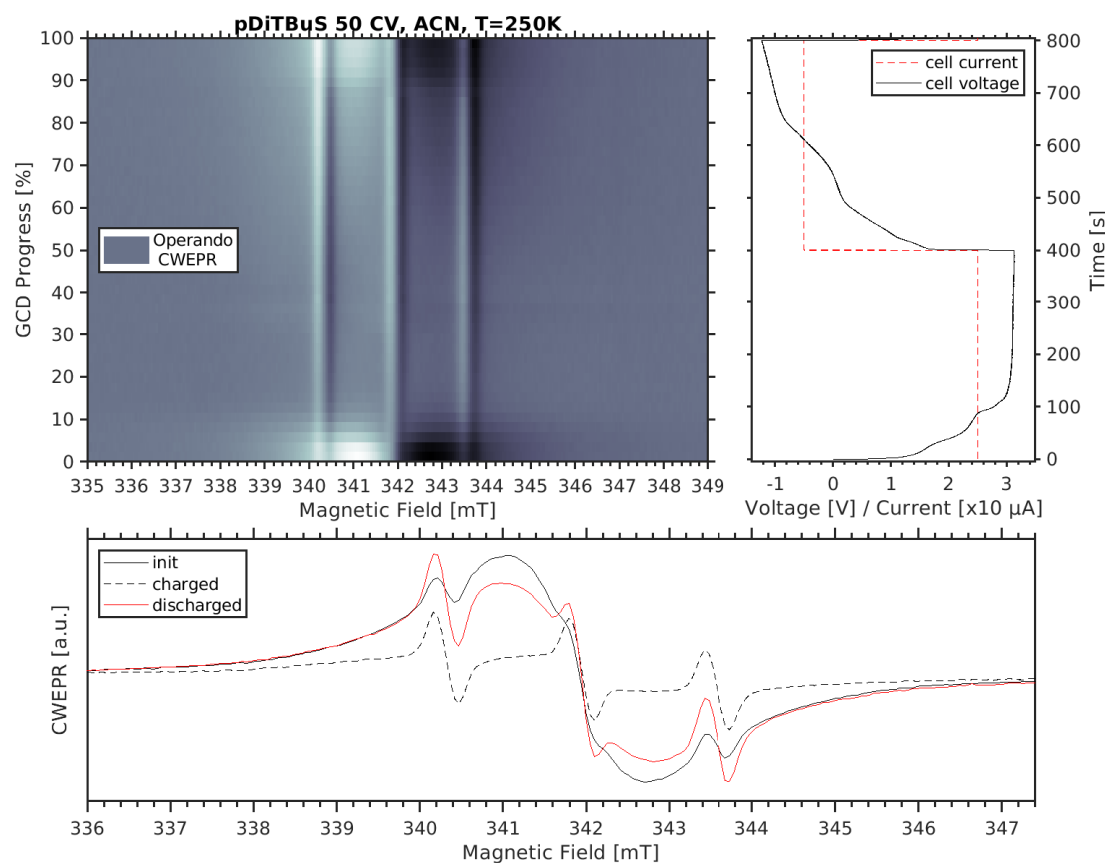


Figure 3.3: XXX



304 **Chapter 4**

305 **pEPR Spectroscopy of Densely Packed  
306 Nitroxide Radicals**

307 **4.1 Coherent Spin Motion under Pulsed Microwave Field**

308 When a spin system is excited with a microwave pulse, its evolution is described with the set of equations  
309 that is known as the Bloch equations.

310 **4.1.1 Bloch Equations**

311 **4.1.2 Spin Relaxation Times**

312 **4.1.3 Spin Packets**

313 **4.2 Instrumentation**

314 **4.2.1 Pulse Sequences and Measurement Techniques**

315 **The Refocused Spin Echo**

316 The Hahn Echo sequence consists of two pulses, the  $\pi/2$  pulse and the  $\pi$  pulse, separated in time by  $\tau$ :  
317  $\pi/2 - \tau - \pi - \tau - echo$ . Initially, the macroscopic magnetization of the spin system is aligned along  $\vec{B}_0$ :  
318  $\vec{M}_0 = M_Z \vec{e}_Z$ . The  $\pi/2$  microwave pulse has such length  $t_{\pi/2}$  and amplitude  $B_1$  that, during the pulse,  $\vec{M}$   
319 nutates to the  $xy$  plane, where it keeps precessing about  $\vec{e}_Z$  after the end of the pulse. The difference in local  
320 environments for each individual spins in the spin packet, as well as the interactions between the spins, that  
321 make up  $\vec{M}$ , leads to slightly different precession frequencies  $\omega_L^i$  of the spins. After some time  $\tau$ , the dif-  
322 ference in the precession frequencies translates into the differences in phases so that the vector sum of the  
323 excited spins averages down to  $\vec{0}$  for sufficiently long  $\tau$ . In other words, the excited spin packet dephases  
324 with time. The dephasing due to different local spin environments can be reversible if the deviations of the  
325 precession frequencies do not depend on time, as is the case for separated electrons in an inhomogeneous  
326 solid. In such case, a  $\pi$  pulse can be applied to the spin system to flip every single spin in the dephased  
327 spin packet by 180deg in a plane containing  $\vec{e}_Z$ , so that the spins keep precessing in the  $xy$  plane, but the  
328 direction of precession is inverted for them, leading to the effect that is opposite to the initial dephasing.  
329 So a  $\tau$  after the  $\pi$  pulse excites the spin packet, the accumulated phase differences become the smallest and  
330 the packet recovers its macroscopic magnetization  $\vec{M}$  that oscillates in the  $xy$  plane with  $\langle \omega_L^i \rangle$  and can be  
331 detected. The recovered  $\vec{M}$  at  $t = \tau$  after the  $\pi$  pulse is called the refocused spin echo. The difference in  $\omega_L^i$   
332 leads to a further dephasing of the considered spin packet and to the vanishing of  $\vec{M}$ .

333

334 **Spin Echo Decay and Phase Memory Time**

335 **Inversion Recovery and Spin-Lattice Relaxation Time**

336 **4.2.2 Broad-Band Excitation and Instantaneous Diffusion**

337 In Section /// it is shown that in a densely packed radical system, as in a TEMPO-Salen cathode film, the  
 338 phase memory time can be shorter than  $T_m \leq 100$  ns. That is, the spin echo is decaying by  $e \approx 3$  at  
 339  $t = 100$  ns. The short phase memory time limits the duration of the pulse sequence at which the echo is  
 340 detectable. For a  $\pi/2 - \tau - \pi - \tau - \text{echo}$  sequence, with a hardware limitation on  $\tau \geq t_d \approx 100$  ns, the pulse  
 341 sequence is longer than  $t > 200$  ns. By this time, the spin echo decreases by  $e^2 \approx 7$  and may be comparable  
 342 to noise. The limitations imposed by the finite  $T_m$  and  $t_d$  force one to use shorter microwave pulses.

343 A short microwave pulse may have a spectral width comparable to the width of the observed spectrum.  
 344 According to the Fourier theorem, the spectral width of a pulse is inversely proportional to the pulse length:  
 345  $\Delta\omega \sim 1/t_p$ . A spectrum of a 100 ns long rectangular pulse shown in Figure /// is ///MHz wide (FWHM).

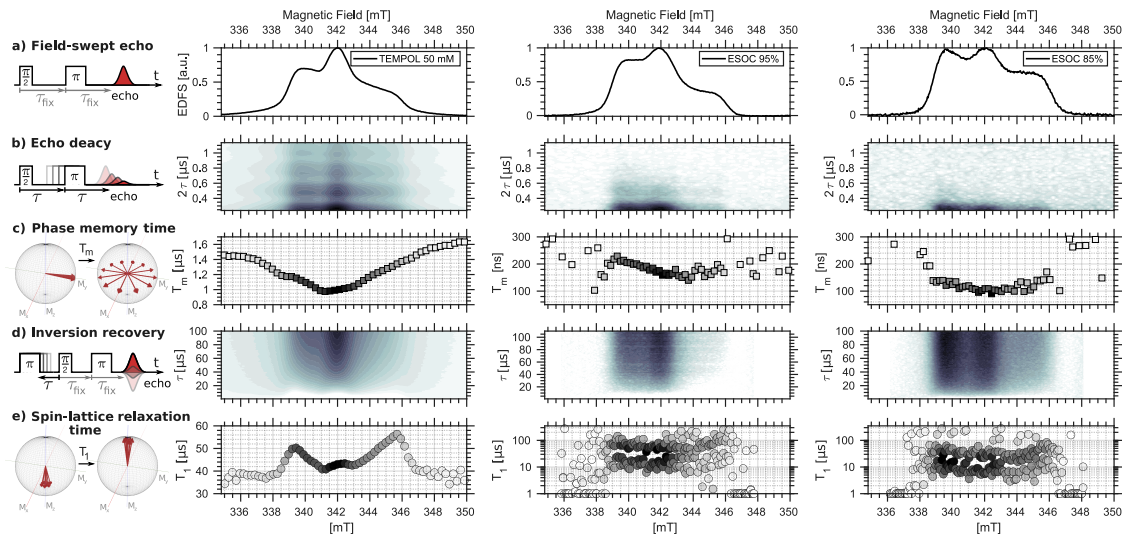


Figure 4.1: XXX

346 **4.3 Pulsed EPR Spectroscopy of a charged pDiTBuS Cathode film**

347 **4.3.1 Field Swept Echo of a charged pDiTBuS Cathode film**

348 **4.3.2 Estimation of Local Spin Concentrations with Instantaneous Diffusion**

349 **4.3.3 Spin Relaxation in a charged pDiTBuS Cathode Film**

350 **4.3.4 Padé-Laplace Deconvolution of Echo Decay Transients**

351 **4.3.5 Detection of Domains with Poor Conductivity**

352 **4.3.6 Towards Imaging of Spin Concentration in Battery Electrodes**

353 One can obtain a spatially resolved image of the spin concentrations inside a battery electrode by encoding  
 354 the position with a gradient of the magnetic field. With the procedure described in Section 4.3.5 and  
 355 using a pair of electromagnetic coils to superimpose a gradient of  $B_0$  one can not only measure the spin  
 356 concentrations that are present in the electrode, but also to locate the electrochemically inactive domains  
 357 and to visualize the conductive paths throughout the electrode.

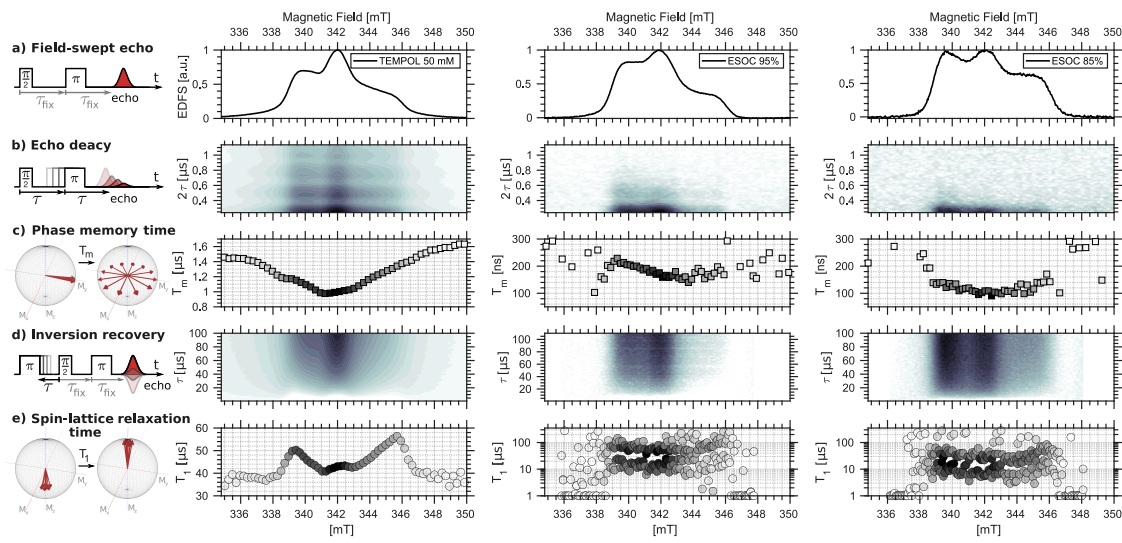


Figure 4.2: XXX

### 358 4.3.7 Unusual Peak Ratios in a Highly Charged Cathode Film



359 **Chapter 5**

360 **Longitudinally Detected Electron  
Paramagnetic Resonance in Systems  
with Short Relaxation Times**

363 LOD lets us look behind the protection pulse.



364 **Chapter 6**

365 **Electrically Detected Magnetic  
366 Resonance on a Cathode of an Organic  
367 Radical Battery**

368 With EDMR we observe the hopping charge as it travels to the charge bearing group through the elec-  
369 trode.

370 **6.0.1 Spin Blockade and Spin-Dependent Recombination**

371 **6.0.2 Instrumentation**

372 **6.0.3 Device Fabrication**

373 **1N4007 Si diode**

374 A commercial 1N4007 p-n Si diode was modified to use as a standard for the EDMR experiments. The  
375 plastic housing of the diode was opened and the copper leads were etched out to reduce the metal content  
376 of the sample that strongly suppresses the  $B_1$  field needed for reaching the resonance condition, and, addi-  
377 tionally, leads to the heating of the sample which affects the current through the diode. The diode with the  
378 opened housing was placed into a droplet of concentrated nitric acid (65%  $\text{HNO}_3$ ) and the etching process  
379 was observed in a microscope. When the copper leads have reduced in size so that only a thin layer of  
380 copper was covering the Si crystal, the etching reaction was stopped with ethanol. Two  $\varnothing 0.1$  mm Ag wires  
381 were used to connect the diode to the detection circuit through the screened coaxial cables. The device was  
382 placed in a  $\varnothing 4.9$  mm OD quartz EPR sample tube.

384 **DPP-DTT Organic Ambipolar Field Effect Transistor**

385 An organic field-effect transistor was fabricated by Z. Wang in the Cavendish Laboratory of the University  
386 of Cambridge in a glovebox filled with Ar. A 3.5 mm wide, 1 mm thick quartz substrate was carrying two  
387 on-substrate meander-shaped Au electrodes as the drain and the source electrodes. A thin film of DPP-DTT  
388 was spin-coated on the on-substrate electrodes. A layer of ????? was spin-coated as the gate isolator on top  
389 of the DPP-DTT film. The Au gate electrode was evaporated onto the isolator layer through a shadow  
390 mask. The metal electrodes were extended with a wire bonder, and soldered to thick Cu wires. The device  
391 was encapsulated in a  $\varnothing 4.9$  mm OD quartz EPR sample tube.

392 **pDiTBuS Organic Radical Battery**

393 **6.0.4 EDMR signal in a 1N4007 Si Diode**

394 **6.0.5 EDMR signal in an Organic Field Effect Transistor**

395 **6.0.6 EDMR signal in a TEMPO-Salen Electrochemical Cell**

396 **6.0.7 Distribution of Current Density in On-Substrate Meander-Shaped Electrodes**

397 Meander-shaped electrodes shown in Figure 6.1 are used to study properties of thin conductive films. The  
398 distribution of electric potential and the current within a film of poor conductivity and a finite thickness be  
399 not obvious.

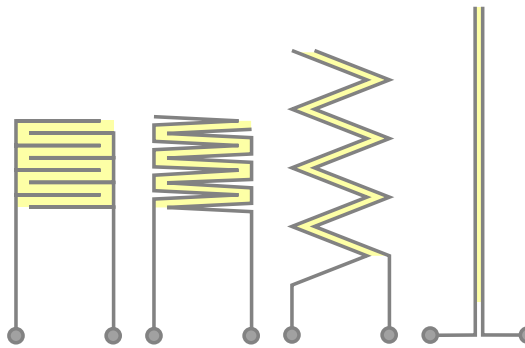


Figure 6.1: Transformation of the meander-shaped electrode grid into two linear electrodes

400 A numerical solution was found to the distribution of the current density  $\vec{j}$  within a film of a finite  
401 thickness, connected by two metal electrodes. Two cases were considered, a thick film and a thin film.

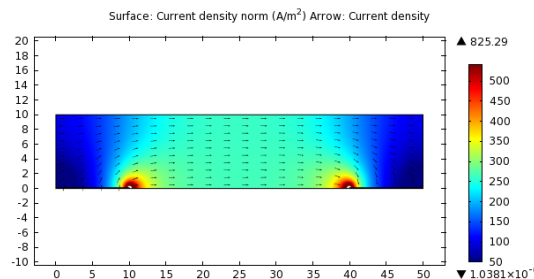


Figure 6.2: Distribution of electric current in a thick polymer film. The current is uniform in the middle of the film. **Let us see, whether we can apply the simple, bulk formula to this structure.**

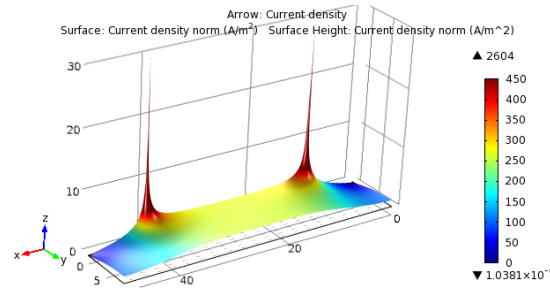


Figure 6.3: Thick film. The current is uniform in the middle of the film. It is better seen on this 3d plot. Let us see, whether we can apply the simple, bulk formula to this structure. I think we do not gain a lot of error by saying that the current is uniform within the whole film.

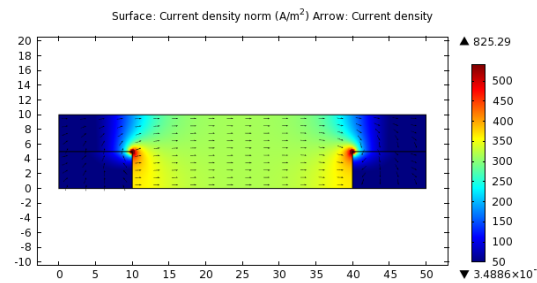


Figure 6.4: Distribution of electric current in an intermediate polymer film

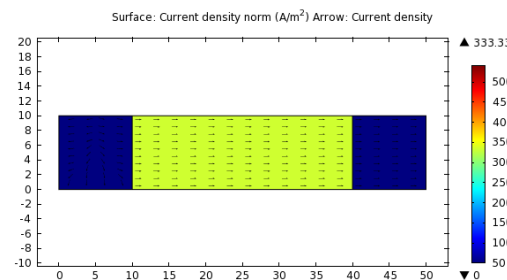


Figure 6.5: Distribution of electric current in a thin polymer film

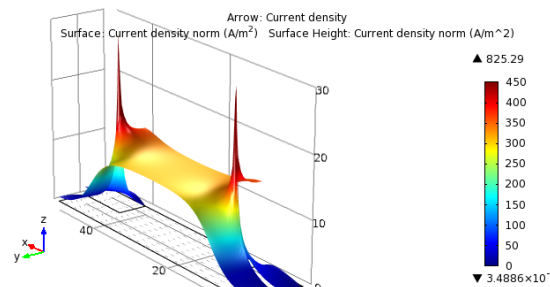


Figure 6.6: Very high values of the computed distribution of the current density in a film of intermediate thickness due to the sharp edges of the contacts.



402

## Chapter 7

403

# The Deep-Trap Model of a 404 TEMPO-Salen Electrode Film

405 A TEMPO-Salen redox conductive film can be seen as a p-type molecular semiconductor enriched with  
406 hole traps. The conductive Salen backbone is carrying positive polarons and bipolarons that delocalize  
407 within the polymer fragments and effectively hop between them. When a polaron, traveling through the  
408 Salen backbone, approaches a charge-bearing TEMPO<sup>•</sup> fragment, it rather hops to it, recombining with  
409 the unpaired electron of the radical. The TEMPO<sup>•</sup> oxidizes and becomes TEMPO<sup>+</sup> which now bears a  
410 positive charge. Therefore, TEMPO<sup>•</sup> is a trap for the positive charge carrier (hole) that is injected into the  
411 poly-Salen network.

412 The charging of a TEMPO-Salen cathode film can be seen as a consequent filling of traps in a hole-  
413 transporting semiconductor. The relative orientations of the spins of the recombining particles defines the  
414 probability of the recombination process. At low SoC, the hole, traveling through the polymer, has many  
415 TEMPO<sup>•</sup> candidates to recombine with. Some of the TEMPO<sup>•</sup> radicals are in the  $|\uparrow\rangle$  state, some are in the  
416  $|\downarrow\rangle$  state, - so the recombination process does not depend on the spin state of the hole, as it can recombine  
417 to the radical in the “appropriate” spin state. At higher SoC, the more TEMPO<sup>•</sup> become occupied with  
418 holes and become TEMPO<sup>+</sup>, the longer distance the hole needs to overcome to meet the TEMPO<sup>•</sup> that has  
419 the “appropriate” spin state. In this case, the recombination process must become spin dependent and an  
420 EDMR signal appears.

421 no edmr data to prove that, yet. The short distance between the TEMPO<sup>•</sup> in the TEMPO-Salen film  
422 leads to the strong exchange interaction between the neighboring TEMPO<sup>•</sup>. That leads to the anti-parallel  
423 alignment of their spins and makes them EPR silent and causes a drastic difference between the Coulomb  
424 counting and the ESOC data. The formation of bipolarons in the Salen backbone and the close packing of  
425 TEMPO<sup>•</sup> may lead to the two-hole-two-electron recombination that can explain the high charging rates of  
426 TEMPO-Salen films.



427

## Chapter 8

428

## Conclusions and Outlook

429

What hasn't worked so far is the EDMR. It would be super cool to see the signal, but my devices don't live that long. LOD also did not work up to now. Adjusting the pulse train rate to the eigenfrequency of the ENDOR coils turned out to be an irresistible obstacle.

430

431



# Bibliography

- [1] Robert Bittl and Stefan Weber. Transient radical pairs studied by time-resolved epr. *Biochimica et Biophysica Acta - Bioenergetics*, 1707:117–126, 2005.
- [2] Nerea Casado and David Mecerreyes. Chapter 1: Introduction to redox polymers: Classification, characterization methods and main applications, 2021.
- [3] Florian Degen and Marius Schütte. Life cycle assessment of the energy consumption and ghg emissions of state-of-the-art automotive battery cell production. *Journal of Cleaner Production*, 330:129798, 2022.
- [4] Boucar Diouf and Christophe Avis. The potential of li-ion batteries in ecowas solar home systems. *Journal of Energy Storage*, 22:295–301, 2019.
- [5] Evgenia Dmitrieva, Marco Rosenkranz, Julia S. Danilova, Evgenia A. Smirnova, Mikhail P. Karushev, Irina A. Chepurnaya, and Aleksander M. Timonov. Radical formation in polymeric nickel complexes with n2o2 schiff base ligands: An in situ esr and uv–vis–nir spectroelectrochemical study. *Electrochimica Acta*, 283:1742–1752, 2018.
- [6] M. Fehr, J. Behrends, S. Haas, B. Rech, K. Lips, and A. Schnegg. Electrical detection of electron-spin-echo envelope modulations in thin-film silicon solar cells. *Physical Review B - Condensed Matter and Materials Physics*, 84:1–5, 11 2011.
- [7] C Fribe and U S Schubert. High-power-density organic radical batteries. *Topics in Current Chemistry*, 375:1–35, 2017.
- [8] Yangyang Fu, Song Lu, Kaiyuan Li, Changchen Liu, Xudong Cheng, and Heping Zhang. An experimental study on burning behaviors of 18650 lithium ion batteries using a cone calorimeter. *Journal of Power Sources*, 273:216–222, 1 2015.
- [9] Walther Gerlach and Otto Stern. Der experimentelle nachweis der richtungsquantelung im magnetfeld. *Zeitschrift für Physik*, 9:348–352, 1922.
- [10] Nicolas Goujon, Nerea Casado, Nagaraj Patil, Rebeca Marcilla, and David Mecerreyes. Organic batteries based on just redox polymers: Abstract. *Progress in Polymer Science*, 122:101449, 2021.
- [11] Cristina Grosu, Chiara Panosetti, Steffen Merz, Peter Jakes, Stefan Seidlmayer, Sebastian Matera, Rüdiger a Eichel, Josef Granwehr, and Christoph Scheurer. Revisiting the storage capacity limit of graphite battery anodes : Spontaneous lithium overintercalation at ambient pressure. *PRX Energy*, 2:1–14, 2023.
- [12] Ting Guan, Shun Sun, Fengbin Yu, Yunzhi Gao, Peng Fan, Pengjian Zuo, Chunyu Du, and Geping Yin. The degradation of licoo2/graphite batteries at different rates. *Electrochimica Acta*, 279:204–212, 2018.
- [13] Takuma Hirasawa, Mika Yoshida, and Shin’ya Obara. Battery control for leveling the amount of electricity purchase in smart-energy houses. *International Journal of Energy Research*, 45:807–823, 2021.

- 468 [14] Q Huang, E D Walter, L Cosimbescu, D Choi, and J P Lemmon. In situ electrochemical-electron  
469 spin resonance investigations of multi-electron redox reaction for organic radical cathodes. *Journal  
470 of Power Sources*, 306:812–816, 2016.
- 471 [15] T Janoschka, M D Hager, and U S Schubert. Powering up the future: Radical polymers for battery  
472 applications. *Adv. Mater.*, 24:6397–6409, 2012.
- 473 [16] Tobias Janoschka, Christian Friebe, Martin D. Hager, Norbert Martin, and Ulrich S. Schubert. An  
474 approach toward replacing vanadium: A single organic molecule for the anode and cathode of an  
475 aqueous redox-flow battery. *ChemistryOpen*, 6:216–220, 2017.
- 476 [17] Tobias Janoschka, Christian Friebe, Martin D. Hager, Norbert Martin, and Ulrich S. Schubert. An  
477 approach toward replacing vanadium: A single organic molecule for the anode and cathode of an  
478 aqueous redox-flow battery. *ChemistryOpen*, 6:216–220, 2017.
- 479 [18] G Jeschke. Deer distance measurements on proteins. *Annual Review of Physical Chemistry*, Vol 63,  
480 63:419–446, 2012.
- 481 [19] Josef Kadlec, Radoslav Cipin, Dalibor Cervinka, Pavel Vorel, and Bohumil Klima. Li-ion accumula-  
482 tors for propulsion system of electric airplane vut 051 ray. *Journal of Solid State Electrochemistry*,  
483 18:2307–2313, 2014.
- 484 [20] Jihyeon Kim, Youngsu Kim, Jaekyun Yoo, Giyun Kwon, Youngmin Ko, and Kisuk Kang. Organic  
485 batteries for a greener rechargeable world. *Nature Reviews Materials*, 8:54–70, 2023.
- 486 [21] Ilia Kulikov, Naitik A. Panjwani, Anatoliy A. Vereshchagin, Domenik Spallek, Daniil A. Lukianov,  
487 Elena V. Alekseeva, Oleg V. Levin, and Jan Behrends. Spins at work: probing charging and dis-  
488 charging of organic radical batteries by electron paramagnetic resonance spectroscopy. *Energy and  
489 Environmental Science*, 15:3275–3290, 2022.
- 490 [22] T. Kushida and J. C. Murphy. Volume dependence of the knight shift in lithium. *Physical Review B*,  
491 21:4247–4250, 1980.
- 492 [23] Fredrik Larsson, Petra Andersson, Per Blomqvist, and Bengt Erik Mellander. Toxic fluoride gas  
493 emissions from lithium-ion battery fires. *Scientific Reports*, 7:1–13, 12 2017.
- 494 [24] Yong Hee Lee, Joo Seong Kim, Jonghyeon Noh, Inhwa Lee, Hyeong Jun Kim, Sunghun Choi, Jeong-  
495 min Seo, Seokwoo Jeon, Taek Soo Kim, Jung Yong Lee, and Jang Wook Choi. Wearable textile  
496 battery rechargeable by solar energy. *Nano Letters*, 13:5753–5761, 2013.
- 497 [25] Chao Li, Ming Shen, and Bingwen Hu. Solid-state nmr and epr methods for metal ion battery re-  
498 search. *Wuli Huaxue Xuebao/Acta Physico - Chimica Sinica*, 36:1–16, 2019.
- 499 [26] Yong Lu and Jun Chen. Prospects of organic electrode materials for practical lithium batteries. *Nature  
500 Reviews Chemistry*, 4:127–142, 2020.
- 501 [27] Tianyi Ma, Siyuan Wu, Fang Wang, Joseph Lacap, Chunjing Lin, Shiqiang Liu, Mohan Wei, Weijian  
502 Hao, Yunshi Wang, and Jae Wan Park. Degradation mechanism study and safety hazard analysis  
503 of overdischarge on commercialized lithium-ion batteries. *ACS Applied Materials and Interfaces*,  
504 12:56086–56094, 2020.
- 505 [28] Praveen Kumar Reddy Maddikunta, Gautam Srivastava, Thippa Reddy Gadekallu, Natarajan Deepa,  
506 and Prabadevi Boopathy. Predictive model for battery life in iot networks. *IET Intelligent Transport  
507 Systems*, 14:1388–1395, 2020.
- 508 [29] Christoph Meier, Jan Behrends, Christian Teutloff, Oleksandr Astakhov, Alexander Schnegg, Klaus  
509 Lips, and Robert Bittl. Multi-frequency edmr applied to microcrystalline thin-film silicon solar cells.  
510 *Journal of Magnetic Resonance*, 234:1–9, 2013.

- 511 [30] Alice J. Merryweather, Quentin Jacquet, Steffen P. Emge, Christoph Schnedermann, Akshay Rao,  
512 and Clare P. Grey. Operando monitoring of single-particle kinetic state-of-charge heterogeneities and  
513 cracking in high-rate li-ion anodes. *Nature Materials*, 21:1306–1313, 2022.
- 514 [31] S Muench, A Wild, C Friebe, B Haupler, T Janoschka, and U S Schubert. Polymer-based organic  
515 batteries. *Chemical Reviews*, 116:9438–9484, 2016.
- 516 [32] K Nakahara, S Iwasa, M Satoh, Y Morioka, J Iriyama, M Suguro, and E Hasegawa. Rechargeable  
517 batteries with organic radical cathodes. *Chem. Phys. Lett.*, 359:351–354, 2002.
- 518 [33] Arvid Niemöller, Peter Jakes, Rüdiger A. Eichel, and Josef Granwehr. In operando epr investigation  
519 of redox mechanisms in licoo<sub>2</sub>. *Chemical Physics Letters*, 716:231–236, 2019.
- 520 [34] Arvid Niemöller, Peter Jakes, Svitlana Eurich, Anja Paulus, Hans Kungl, Rüdiger A. Eichel, and  
521 Josef Granwehr. Monitoring local redox processes in lini0.5mn1.5no<sub>4</sub> battery cathode material by in  
522 operando epr spectroscopy. *Journal of Chemical Physics*, 148:1–10, 2018.
- 523 [35] Hiroyuki Nishide, Kenichiro Koshika, and Kenichi Oyaizu. Environmentally benign batteries based  
524 on organic radical polymers. volume 81, pages 1961–1970, 2009.
- 525 [36] Naoki Nitta, Feixiang Wu, Jung Tae Lee, and Gleb Yushin. Li-ion battery materials: Present and  
526 future. *Materials Today*, 18:252–264, 2015.
- 527 [37] Jens F. Peters, Manuel Baumann, Benedikt Zimmermann, Jessica Braun, and Marcel Weil. The  
528 environmental impact of li-ion batteries and the role of key parameters – a review. *Renewable and  
529 Sustainable Energy Reviews*, 67:491–506, 2017.
- 530 [38] Anna Pražanová, Vaclav Knap, and Daniel Ioan Stroe. Literature review, recycling of lithium-ion  
531 batteries from electric vehicles, part i: Recycling technology. *Energies*, 15:1–29, 2022.
- 532 [39] Kevin J. Rhodes, Roberta Meisner, Melanie Kirkham, Nancy Dudney, and Claus Daniel. In situ xrd of  
533 thin film tin electrodes for lithium ion batteries. *Journal of The Electrochemical Society*, 159:A294–  
534 A299, 2012.
- 535 [40] K. M. Salikhov, S. A. Dzuba, and A. M. Raitsimring. The theory of electron spin-echo signal decay  
536 resulting from dipole-dipole interactions between paramagnetic centers in solids. *Journal of Magnetic  
537 Resonance*, 42:255–276, 1981.
- 538 [41] K M Salikhov and N E Zavoiskaya. Zavoisky and the discovery of epr, 2015.
- 539 [42] A Schweiger and G Jeschke. *Principles of Pulse Electron Paramagnetic Resonance*. Oxford University  
540 Press, 2001.
- 541 [43] A Schweiger and G Jeschke. *Principles of Pulse Electron Paramagnetic Resonance*. Oxford University  
542 Press, 2001.
- 543 [44] Yongchao Shi and Mingxue Tang. Nmr/epr investigation of rechargeable batteries. *Wuli Huaxue  
544 Xuebao/Acta Physico - Chimica Sinica*, 36:1–13, 2019.
- 545 [45] Hiroyuki Takeo Nishide and Suga. Organic radical battery. *Journal of the Society of Mechanical  
546 Engineers*, 110:194–195, 2007.
- 547 [46] Yu. V. Toropov, S. A. Dzuba, Yu. D. Tsvetkov, V Monaco, F Formaggio, M Crisma, C Toniolo, and  
548 J. Raap. Molecular dynamics and spatial distribution of toac spin-labelled peptaibols studied in glassy  
549 liquid by echo-detected epr spectroscopy. *Applied Magnetic Resonance*, 15:237–246, 1998.
- 550 [47] Anatolii. A. Vereshchagin, Daniil A. Lukyanov, Ilia R. Kulikov, Naitik A. Panjwani, Elena A. Alek-  
551 seeva, Jan Behrends, and Oleg V. Levin. The fast and the capacious: A [ni(salen)]-tempo redox-  
552 conducting polymer for organic batteries. *Batteries & Supercaps*, 4:336–346, 2020.

- 553 [48] Anatoliy A. Vereshchagin, Arseniy Y. Kalnin, Alexey I. Volkov, Daniil A. Lukyanov, and Oleg V.  
554 Levin. Key features of tempo-containing polymers for energy storage and catalytic systems. *Energies*,  
555 15:1–50, 2022.
- 556 [49] Yuan Xie, Kai Zhang, Yusuke Yamauchi, Kenichi Oyaizu, and Zhongfan Jia. Nitroxide radical poly-  
557 mers for emerging plastic energy storage and organic electronics: Fundamentals, materials, and ap-  
558 plications. *Materials Horizons*, 8:803–829, 2021.
- 559 [50] Chengjian Xu, Qiang Dai, Linda Gaines, Mingming Hu, Arnold Tukker, and Bernhard Steubing.  
560 Future material demand for automotive lithium-based batteries. *Communications Materials*, 1:1–10,  
561 2020.
- 562 [51] Hyun Deog Yoo, Elena Markevich, Gregory Salitra, Daniel Sharon, and Doron Aurbach. On the  
563 challenge of developing advanced technologies for electrochemical energy storage and conversion.  
564 *Materials Today*, 17:110–121, 2014.
- 565 [52] E K Zavoisky. Paramagnetic relaxation of liquid solutions for perpendicular fields. *Zhur. Eksperiment.*  
566 *i Theoret. Fiz.*, 15:344–350, 1945.
- 567 [53] Clara Zens, Christian Fribe, Ulrich S. Schubert, Martin Richter, and Stephan Kupfer. Tailored charge  
568 transfer kinetics in precursors for organic radical batteries – a joint synthetic-theoretical approach.  
569 *ChemSusChem*, e202201679:1–14, 2022.
- 570 [54] Guangxu Zhang, Xuezhe Wei, Siqi Chen, Guangshuai Han, Jiangong Zhu, and Haifeng Dai. Investi-  
571 gation the degradation mechanisms of lithium-ion batteries under low-temperature high-rate cycling.  
572 *ACS Applied Energy Materials*, 5:6462–6471, 2022.
- 573 [55] Qingsong Zhang, Tiantian Liu, and Qiong Wang. Experimental study on the influence of different  
574 heating methods on thermal runaway of lithium-ion battery. *Journal of Energy Storage*, 42:1–9, 10  
575 2021.